








RESEARCH ARTICLE | AUGUST 22 2023

A convenient switch design for high time resolution and energy resolution in ion velocity imaging **FREE**

Tongpo Yu ; Xinlang Yang; Zhi Gao ; Baokun Shan ; Lei Xu; Xiaoguo Zhou  ; Shilin Liu  



Rev Sci Instrum 94, 083307 (2023)

<https://doi.org/10.1063/5.0166280>



View
Online



Export
Citation

CrossMark

Articles You May Be Interested In

Photon counting phosphorescence lifetime imaging with TimepixCam

Rev Sci Instrum (January 2017)

Design and characterization of a velocity-map imaging apparatus for low-energy photo-ion spectroscopy using magneto-optically trapped atoms

Rev Sci Instrum (April 2021)

Photodissociation dynamics of H_2S^+ near 325 nm

Chinese Journal of Chemical Physics (June 2023)

A convenient switch design for high time resolution and energy resolution in ion velocity imaging

Cite as: *Rev. Sci. Instrum.* **94**, 083307 (2023); doi: [10.1063/5.0166280](https://doi.org/10.1063/5.0166280)

Submitted: 4 July 2023 • Accepted: 3 August 2023 •

Published Online: 22 August 2023



View Online



Export Citation



CrossMark

Tongpo Yu,^{1,2}  Xinlang Yang,²  Zhi Gao,³  Baokun Shan,²  Lei Xu,²  Xiaoguo Zhou,^{2,a)}  and Shilin Liu^{2,a)} 

AFFILIATIONS

¹ Department of Physics, Hefei University of Technology, Hefei 230009, China

² Department of Chemical Physics, University of Science and Technology of China, Hefei 230026, People's Republic of China

³ Hefei National Laboratory for Physical Sciences at the Microscale, University of Science and Technology of China, Hefei 230026, People's Republic of China

^{a)} Authors to whom correspondence should be addressed: xzhou@ustc.edu.cn and slliu@ustc.edu.cn

ABSTRACT

Time-sliced velocity map imaging (VMI) has extensively been applied in photodissociation dynamics studies, thanks to its unique advantages, such as high energy resolution and no requirement of inverse Abel or Hankel transformations. However, its time resolution is generally insufficient for distinguishing adjacent m/z ions with a certain kinetic energy due to the overlapping of time-of-flight distributions. Herein, we have made a novel and convenient switch design for the common ion optics in three-dimensional (3D) VMI. By simply introducing two additional resistors out of the vacuum chamber, the strength ratio of the extraction and acceleration fields is easily changed from 3D VMI to two-dimensional (2D) VMI under optimized conditions, as well as a significant extension of free drift length, leading to a higher time resolution while maintaining the high energy resolution. As a result, 2D and 3D VMI can be quickly switched without breaking the vacuum and replacing the electrostatic plates.

Published under an exclusive license by AIP Publishing. <https://doi.org/10.1063/5.0166280>

I. INTRODUCTION

Since Chandler and Houston first reported the ion imaging method based on linear Wiley–McLaren time-of-flight (TOF) mass spectrometry in 1987,¹ this approach has attracted much attention and a lot of efforts have been made to improve its performance. By using circular ring electrodes to form electrostatic lenses, Eppink and Parker proposed the velocity map imaging (VMI) in 1997,² in which the distortions and transmission losses arising from the grid electrodes were eliminated. Much more importantly, under the VMI conditions, all charged particles with the same initial velocity vector could be focused onto the same position of a 2D position-sensitive detector, independent of their initial positions in the ionization region, thus improving the image resolution significantly. In addition, VMI offers more details on velocity and angular distributions of charged particles than ion imaging and mass spectrometry techniques. Due to these unique advantages, VMI, therefore, has widely been applied in diverse research fields related to molecular reaction dynamics.^{3–6}

In a conventional VMI experiment, the recorded images for each m/z are the 2D projection of the full 3D velocity distribution, the so-called 2D velocity imaging. For dissociation experiments using linearly polarized laser parallel to the detector, the velocity distribution has cylindrical symmetry. In this case, only a central “slice” of the Newton sphere of the incoming ion image is necessary to be recorded, and then, the 3D velocity distribution can be obtained using the 2D image reconstruction with inverse Abel or Hankel transformations.⁷ For achieving a better 2D image resolution, some special designs on VMI lens (named as “slice imaging”) have been reported, in which the 3D distribution is measured directly from a series of 2D sliced images without the Abel inversion, e.g., pulsed-field slicing,⁸ optical slicing,⁹ and Doppler slicing.^{10,11} Moreover, in systems without cylindrical symmetry, such as the crossed molecular beam scattering experiments, Lin *et al.* applied a weak extraction field to spread the ion turnaround time and used a fast gated charge-coupled device (CCD) camera to record the time-sliced ion images.¹² Recently, using new in-vacuum pixel detectors like TimepixCam, efficient slice imaging of multi-mass ions has been

achieved.^{13–15} In addition, a few special designs have been reported, e.g., a large aperture magnification lens for VMI¹⁶ and a penetration electric field to construct a low extraction.¹⁷ In addition, “event counting,”¹⁸ “*p*Basex,”¹⁹ and “megapixel imaging”²⁰ as enhanced algorithms have been used to improve the velocity resolution. Some reviews have summarized the details and recent advances of the VMI approach.^{6,21–23}

In general, a weak extraction field facilitates the expansion of ion clouds, leading to a better energy resolution in 3D VMI measurements using the time-slicing method, but it is not conducive to obtaining a good time resolution (or a mass-to-charge resolution of TOF mass spectrometer). This contradiction becomes a crucial constraint in some VMI experiments, such as photodissociation dynamics of hydrogen sulfide cations,²⁴ where the mass peak of HS• radical and sulfur atom fragments might overlap due to wide kinetic energy released distributions (KERDs) in dissociation. As a result, accurate measurements of branching ratio and sliced image of these fragments are inevitably affected. Thus, how to achieve a high time resolution and a high energy resolution simultaneously in VMI is still a challenge to date.

In this work, we proposed a fast switching method of 3D and 2D VMI in one apparatus without the need to break the vacuum and reconnect the resistors. The whole ion optics is mainly composed of three stages, i.e., extraction, acceleration, and soft focusing. By switching the control resistors readily outside the vacuum, the ion optics can work in 2D and 3D VMI modes alternatively. A few benchmark experiments of VMI have been performed to examine its performance.

II. APPARATUS

A. Ion optics

For obtaining a high energy resolution in slice imaging, ion Newton spheres need to be expanded significantly along both parallel and perpendicular directions of flight. Thus, a weak extraction field is usually used to spread the ion turnaround time and broaden the TOF distribution, and meanwhile, relatively slow changes in the electric field gradients are necessary to get a soft focusing effect in the 3D VMI design. On the contrary, a strong extraction field and a relatively large ratio of the field strengths of extraction and acceleration stages are often applied in 2D VMI experiments, as Eppink and Parker did.² In this case, the high time resolution is easily achieved.

Considering these characteristics, a conventional ion optics of 3D VMI was adopted as the basic framework of our ion imaging, which was similar to the multi-plate designs of Lin *et al.*¹² and Wu *et al.*²⁵ Figure 1 shows the geometric diagram of the current VMI device. A total of 26 circular stainless steel plates (an outer diameter of 72 mm and a thickness of 1 mm) constitute an electrostatic field with cylindrical symmetry along the direction of ion flight, which are connected with the precision resistors to divide voltages. The distance from the ionization region to the detector is about 48.0 cm. The two repeller electrodes of the ionization region (noted as #2 and #3 in Fig. 1) are separated by aluminum oxide spacers of 12 mm length, and the spacers between the other adjacent electrodes are of 6 mm. All electrodes are totally open without any grids, to avoid the distortion of ion trajectories by grids. The size of the center hole for electrodes is gradually increased from 10 to 35 mm, as shown in Fig. 1. In addition, a shielding ring (an

inner diameter of 48 mm and a length of 5 mm) is connected with each electrode, to efficiently eliminate the influences of surrounding electric fields. One grid is mounted 1.5 mm in the front of the detector surface (in Fig. 1), to shield from the gated high-voltage electric field of the detector. In such a short distance, the distortion of ion trajectories can be ignored. The similar design was successfully employed in our previous threshold photoelectron-photoion coincidence apparatus.²⁶

At a relatively weak extraction field of 37 V cm⁻¹, Fig. 2(a) shows the potential configuration of the current 3D VMI and ion trajectories simulated with SIMION 3D (version 8.0, Scientific Instrument Services), where the initial velocity of ions (*m/z* 32) perpendicular to the flight axis is 1736 m s⁻¹ ($E_T = 0.5$ eV). Table I lists the precision resistors of the connections between adjacent electrodes. The whole ion optics is roughly divided into three regions: the extraction stage is composed of electrodes #1, #2, and #3, where #1 is used to install the skimmer (1 mm diameter, Beam Dynamics) and to shield the influence of external electric fields, such as the valve; electrodes #4 to #9 form the acceleration stage, where the gradient of the electric field is gradually decreased to 32 V cm⁻¹; the third stage plays the role of soft focusing with a further slow increase in the electric field gradient. The free drift length is 326 mm.

To obtain the high time resolution in a Wiley–McLaren TOF mass spectrometry configuration, a relatively strong extraction field is necessary for compressing the turnaround time of ions. In addition, a large ratio of the electric field strengths of the extraction and acceleration stages is also required for 2D VMI. Thus, without a change in the ion optics geometry mentioned above, we adopted a clever method to achieve such changes in electric fields. In particular, an additional resistor (R_2') was connected in parallel to electrodes #2 and #3 outside the vacuum, and meanwhile, another resistor (R_8') was linked in parallel to electrodes #8 and #9. By grounding R_8' at the other end, we thus increased the ratio of the electric field strengths of the extraction and acceleration stages to 1:5 from 1:2 in the 3D VMI mode. The drift length is extended to 447 mm in this case, owing to the removal of the soft focus region. With the same hardware configuration shown in Fig. 1, the VMI effect of this fast switch is compared, as shown in Fig. 2. Therefore, a convenient switch design for 2D (a high time resolution) and 3D (a high energy resolution) in one conventional VMI apparatus is achieved, without breaking the vacuum and reconnecting the resistors.

Taking into account the small size of focused laser beam (propagating in the *X* direction in Fig. 1) in photoionization, the initial spread of the ion cloud along the *Z* direction is usually less than 0.5 mm. Thus, an ionization region of $4 \times 4 \times 0.5$ mm³ is chosen in trajectory simulations. The radial coordinate of a velocity map image is proportional to the velocity component (v_x) of the ion in the image plane. As one of the most important mapping characteristics, the magnification factor of VMI is defined as $N = r/r'$, where r is the ring radius of the ion image on the detector, and $r' \equiv v_x \times t$ (t is the flight time). Using the *m/z* 32 ions and the total electric field of 1600 V as an example, Fig. 3 shows the simulated magnification factors in the 2D and 3D VMI modes, both exhibiting good linearity. The simulated N value is 0.74 for the 3D VMI design, indicating a reduced ion velocity map image due to the soft focusing effect. In fact, this reduced imaging facilitates full utilization of the limited size of the detector [efficient diameter is 40 mm for micro-channel plates (MCPs) in our system], while maintaining the high energy resolu-

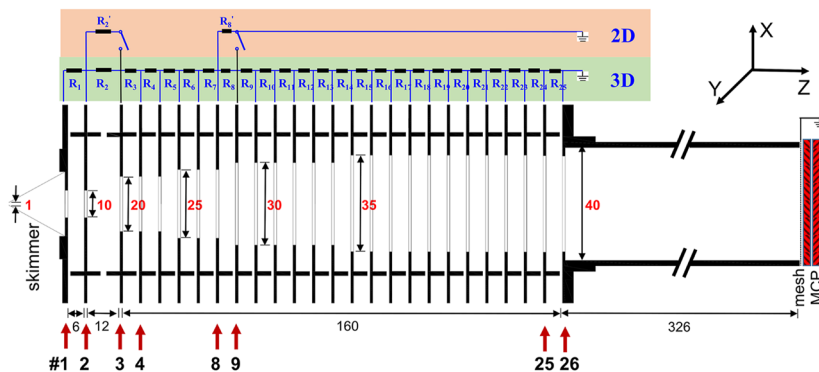


FIG. 1. Geometry and resistor connection diagram of the current VMI device.

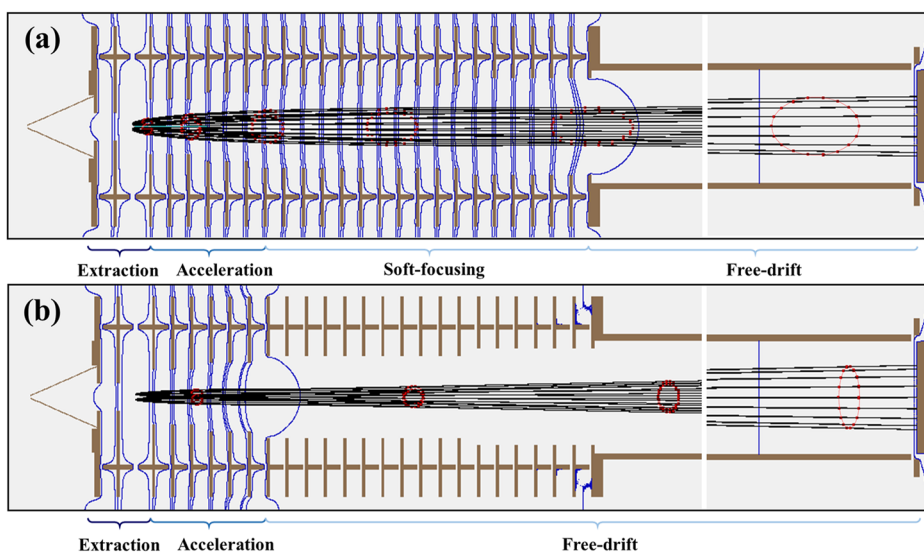


FIG. 2. Potential configuration and simulated trajectories of ions (m/z 32, with the initial velocity perpendicular to the flight axis of 1736 m s^{-1} , E_T of 0.5 eV), where the total voltage is 1600 V for ion optics, in the (a) 3D and (b) 2D VMI modes. The red dotted circles represent the spatial shape of the ion cloud along the flight axis.

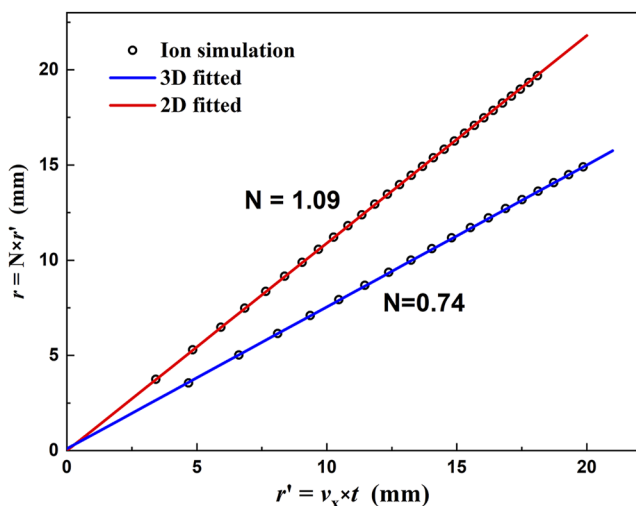
tion. As shown by the red dotted circles in Fig. 2(a), a flat ellipsoidal shape is observed for the ion cloud at the end of the drift tube under these conditions, which enables time-slicing measurements. In contrast, the N value is increased to 1.09 in the 2D VMI mode with an extraction field of 140.5 V cm^{-1} . It is worth noting that the total electric field is maintained at 1600 V in both the 2D and 3D VMI modes. As shown in Fig. 2(b), the TOF distribution is compressed due to the high extraction field in the 2D mode, resulting in a vertical ellipsoidal shape of ion clouds before reaching the detector. The overlapping of adjacent ion spheres with a relatively high kinetic energy can be efficiently avoided. As a result, we can directly measure the accurate branching ratios of various fragments, while achieving a satisfactory energy resolution owing to the enlarged imaging effect.

Table II summarizes the simulated time resolution and energy resolutions in the 3D and 2D VMI modes for the m/z 32 ions. For the ions with an initial kinetic energy of 0.2, 0.4, and 0.6 eV, the TOF

width (Δt) in the 3D mode is calculated to be 220, 300, and 370 ns, respectively. Such a large Δt represents a poor resolving power of the mass spectrometer, which is obviously insufficient for distinguishing the fragment ions of adjacent m/z in this application scenario. In contrast, the relatively high energy resolution ($\Delta E_T/E_T$) of the 3D VMI design is achieved as 1.65% for 0.2 eV, 0.40% for 0.4 eV, and 0.41% for 0.6 eV, respectively. For comparison, in the 2D VMI mode, the TOF distributions for the ions with E_T of 0.2, 0.4, and 0.6 eV are reduced to 70, 90, and 110 ns, respectively. This significantly improved time resolution provides a chance to separate the adjacent mass peaks with a certain kinetic energy. Moreover, the energy resolution ($\Delta E_T/E_T$) is simulated as 0.86% for 0.2 eV, 0.19% for 0.4 eV, and 0.36% for 0.6 eV, which is even slightly higher than the results of the 3D VMI design. In other words, both 2D and 3D VMI designs in the current ion optics can ensure the relatively high energy resolution in ion imaging.

TABLE I. Optimized precision resistors (in k Ω) between adjacent electrodes in the VMI design.

R ₁	R ₂	R ₃	R ₄	R ₅	R ₆	R ₇	R ₈	R ₉	R ₁₀	R ₁₁	R ₁₂	R ₁₃	R ₁₄
180	350	180	170	240	200	280	280	280	360	360	360	420	420
R ₁₅	R ₁₆	R ₁₇	R ₁₈	R ₁₉	R ₂₀	R ₂₁	R ₂₂	R ₂₃	R ₂₄	R ₂₅	R _{2'}	R _{8'}	
420	530	530	530	720	720	720	720	840	840	840	300	1145	

**FIG. 3.** Magnification factors of the current ion velocity map imaging in the 2D and 3D modes.

B. Detector

For detecting ions, a micro-channel plate (MCP) assembly (Hamamatsu, F2225-21P-Y003) was used in our experiments, in which two MCPs (a 42 mm diameter effective area) in the chevron geometry were coupled to a phosphor screen (P47). A charge-coupled device (CCD) camera (LaVision, Imager QE) was used to record the ion images on the screen. In time-slicing measurements, a pulsed voltage of -1700 V with the effective pulse width of ~ 40 ns was applied to the incident surface of the first MCP as a mass gate, which was offered by a high voltage pulse generator (DEI, PVX-4140). As indicated in Table II, the TOF widths of the fragment ions usually increase to several hundred nanoseconds due to the kinetic energy release; thus, the current pulse width was narrow enough to achieve the time-slicing effect. To shield the electric field of the detector from ion trajectories, a grid was placed just at the front of the incident surface of the MCPs (Fig. 1). The ion event counting method¹⁸ was used in the measurement processes, further improving the image resolution.

III. EXPERIMENT

A. Calibration for velocity map imaging

The dissociative photoionization of O₂ at 224.999 nm is commonly used as a calibration for VMI systems, since the kinetic energy

released distribution of the O⁺ fragment ions has been studied very well.^{12,25,27,28} Figure 4 shows the time-sliced image of O⁺ using the current VMI imaging system in the 3D VMI mode. The great linear relationship between the O⁺ speed and the ring radius is clearly shown, verifying our 3D VMI functionality. Notably, we adopted the polarization of the incident laser at the magic angle in this experiment, in order to test the homogeneity of the imaging system. As the radial coordinate of a velocity map image is proportional to the ion velocity component in the image plane, the calibrated factor for the image radius and the kinetic energy (E_T) of ions is determined from the image shown in Fig. 4. In addition, the average resolution ($\Delta E_T/E_T$) of the current system in the 3D VMI mode is derived to be better than 1.4%, which is generally consistent with the simulated results in Table II.

B. Time resolution

Time resolution (i.e., mass resolution) is one of the most important parameters for a TOF mass spectrometer. One aim of the present VMI design is to obtain a high time resolution while recording ion imaging with a high energy resolution. Thus, we used the photodissociation of carbonyl sulfide (OCS) as a benchmark to assess the current system, according to its well-known dynamic information.^{29–32} In the photodissociation of OCS at 230 nm, the CO($X^1\Sigma^+$) fragment and the S(1D or 3P) atom are formed. Then, the CO⁺ cations can be produced by (2 + 1) resonance-enhanced multiphoton ionization (REMPI) at this wavelength. As shown in Fig. 5, the CO⁺ peak can be clearly observed in the TOF mass spectra in both the 2D and 3D VMI modes. With the total TOF voltage of 1600 V, the full width at half maximum (FWHM) of the CO⁺ peak in the TOF spectra in the 3D VMI optics is 230 ns (the extraction filed of 37 V cm⁻¹), while it is reduced to 60 ns in the 2D mode according to the significantly enhanced extraction filed of 140.5 V cm⁻¹. These results perfectly agree with the simulated data given in Table II. This greatly improved time resolution is due to the reduced turnaround time in the higher extraction field.

C. Ion velocity map imaging

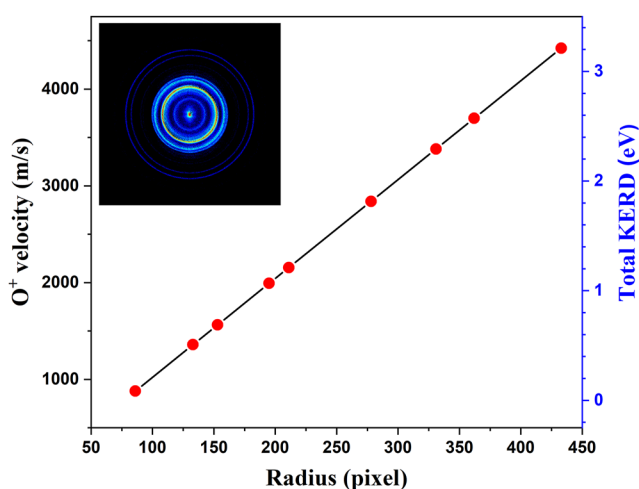
Figure 6(a) shows the time-sliced ion image of the CO($X^1\Sigma_g^+$, $v = 0, J = 66$) fragment in the 3D VMI mode, where the light vector ϵ is along the vertical direction in the image plane as shown by the yellow arrows. For comparison, the raw velocity map image recorded in the 2D VMI mode is shown in Fig. 6(b) and the corresponding 3D distribution derived from the inverse Abel transformation is shown in Fig. 6(c).

As shown in Fig. 6, the image patterns recorded in both the 2D and 3D VMI modes are almost identical, except that the noise is

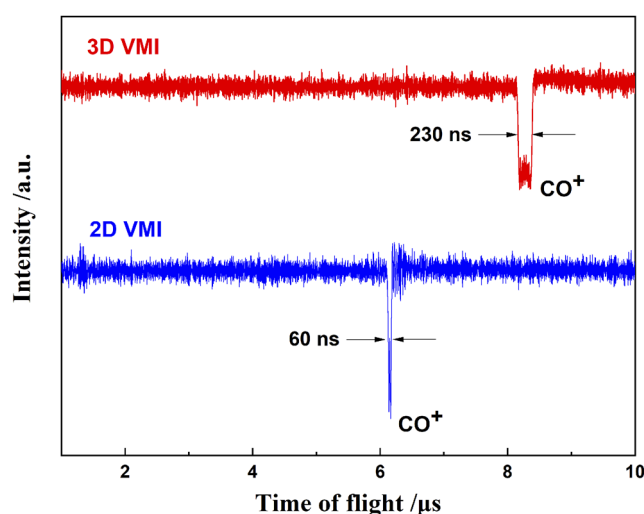
TABLE II. Energy and time resolutions of ion imaging (m/z 32) on the detector derived from the ion trajectory simulations with various initial kinetic energies (E_T), where the extraction field is 37 V cm^{-1} in the 3D VMI mode and 80 V cm^{-1} in the 2D VMI mode. The ionization region is $4 \times 4 \times 0.5 \text{ mm}^3$ (X - Y - Z axis).

Mode	E_T (eV)	Time of flight (μs)		TOF width Δt (ns)	Radius (mm)		ΔR (mm)	Energy resolution ($\Delta E_T/E_T$ %) ^a
		Max.	Min.		Max.	Min.		
3D	0.2	8.62	8.42	220	7.28	7.16	0.12	1.65
	0.4	8.67	8.37	300	10.20	10.16	0.04	0.40
	0.6	8.70	8.33	370	12.48	12.43	0.05	0.41
2D	0.2	6.86	6.79	70	8.14	8.07	0.07	0.86
	0.4	6.87	6.78	90	10.47	10.45	0.02	0.19
	0.6	6.88	6.77	110	14.05	14.00	0.05	0.36

^aUsually, the energy resolution ($\Delta E_T/E_T$) should be half of the radius resolution ($\Delta R/R$), since the R is linearly dependent on the ion velocity v_x . However, the ΔR values in this table are full width of ring radius, and thus, $\Delta E_T/E_T$ equals to be $\Delta R/R$ here.

**FIG. 4.** Time-sliced image of the O^+ fragment produced in the dissociative photoionization of O_2 at 224.999 nm, where the polarization of the incident laser was set at the magic angle.

accumulated along the centerline in Fig. 6(c) due to the inverse Abel transformation. The inner pattern is dominated by three circles, while the outer one is a single large ring with a bit weaker brightness. Moreover, each circle shows a certain degree of anisotropy. According to the above calibrated factor for the radius and kinetic energy of ions, the interval among the three inner rings corresponds to $\sim 66 \text{ meV}$, which agrees well with the bending vibration ($\nu_2 = 65 \text{ meV}$) of the parent molecule (OCS).^{30–32} Thus, taking into account the dissociation limit of $\text{OCS}(X^1\Sigma_g^+) \rightarrow \text{CO}(X^1\Sigma_g^+, v, J) + \text{S}(^1\text{D})$, the innermost ring to the outer one of the inner pattern is assigned to the ν_2 quantum numbers ($v = 0-2$) in sequence. The existence of the bending excitation is attributed to the thermal distribution of the parent molecules. In addition, the outer weak ring is attributed to the second decomposition channel of $\text{OCS}(X^1\Sigma_g^+) \rightarrow \text{CO}(X^1\Sigma_g^+, v, J) + \text{S}(^3\text{P})$.²⁹

**FIG. 5.** TOF mass spectra of the $\text{CO}(X^1\Sigma_g^+, v = 0, J = 66)$ fragment from the photodissociation of OCS at 229.83 nm, where the red and blue traces are recorded in the 3D and 2D VMI modes, respectively.

D. Corrections on branching ratios derived from the time-sliced imaging

For dissociation of polyatomic molecules, branching ratios along different decomposition pathways to produce the same m/z fragment ions are very important to understand the coupling effects of various electronic states in dissociation dynamics, such as “roaming mechanism.”³³ In a common time-sliced 3D VMI experiment, the kinetic energy release distribution (KERD) can be obtained by integrating a time-sliced image over the angular coordinate. The branching ratio of a specific decomposition channel is then calculated as the fraction of the corresponding distribution intensity in the total KERD. Obviously, the accurate branching ratio needs to be measured at the identical spatial angle ($\Delta\Omega$) for each ring (or speed distribution) in principle. However, as indicated in Fig. 7, the $\Delta\Omega$ values (or $\Delta\phi$) are apparently varied with the ring radius when the mass gate (Δt) is used in experiments. Along with the increase

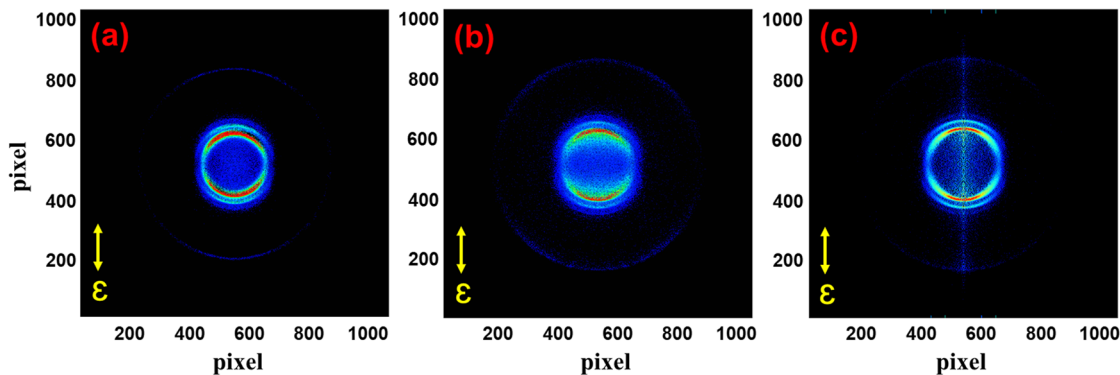


FIG. 6. Ion velocity map imaging of the $\text{CO}(X^1\Sigma_g^+ v=0, J=66)$ fragment produced from the photolysis of OCS at 229.83 nm. (a) The time-sliced 3D VMI image with the mass gate of ~ 40 ns, (b) the raw VMI image in the 2D mode, and (c) the 3D image reconstructed from the inverse Abel transformation.

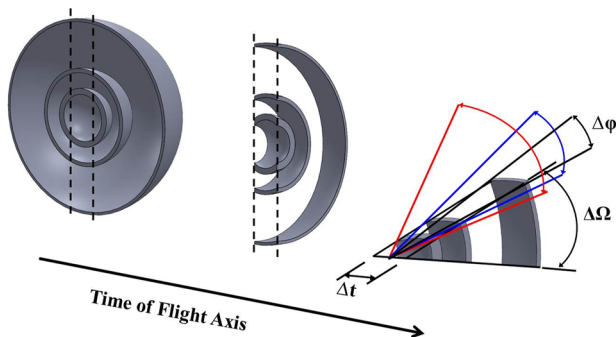


FIG. 7. Schematic diagram for the branching ratio measurement based on the time-sliced image. The center part of the three Newton spheres is cut out by means of a time-gated detector (the so-called mass gate).

in the ring radius, the $\Delta\phi$ value is gradually reduced together with $\Delta\Omega$, meaning that the branching ratios that are directly calculated from the KERD of a time-sliced velocity map image are not accurate enough. The component of the lower kinetic energy will be overestimated in comparison with the higher part. Fortunately, this phenomenon can be avoided in the 2D VMI measurements. Thus, we can evaluate the error of the calculated branching ratio in the time-sliced 3D velocity map image by comparing the 2D and 3D VMI results.

Using the decomposition of OCS at ~ 230 nm as a representative, Fig. 8 shows the comparison of the total KERDs obtained from the time-sliced 3D image [Fig. 6(a)] and the 3D distribution [Fig. 6(c)] derived from the inverse Abel transformation of the 2D velocity map image [Fig. 6(b)]. The branching ratio of the triplet dissociation channel to the product $\text{CO}(X^1\Sigma_g^+, v, J)$ and $\text{S}(^3P)$ is determined to be 12.9% from the common time-sliced image, which is increased to 16.5% using the 2D measurement results. This difference verifies the influence of the $\Delta\Omega$ (or $\Delta\phi$) change on the branching ratio. As a result, a calibration is required when using the time-sliced images to directly calculate the branching ratios. Notably, the calibration factors not only depend on the ring radius

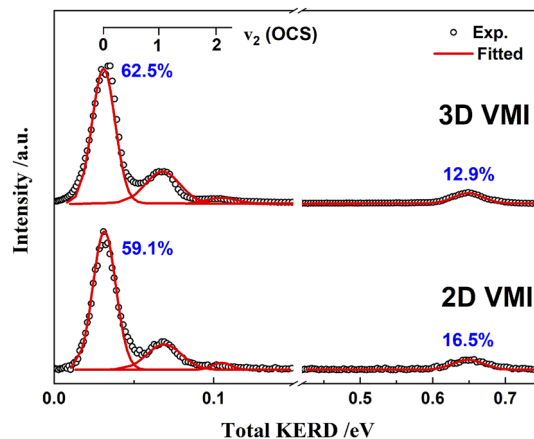


FIG. 8. Comparison of the total KERDs determined from the time-sliced 3D image [Fig. 6(a)] and the 3D distribution [Fig. 6(c)] derived from the inverse Abel transformation of the 2D velocity map image [Fig. 6(b)], as well as the corresponding branching ratios.

but also correlate with the angular distributions (i.e., anisotropy parameter β), since the proportion of the recorded intensity within a mass gate varies with the scattering angle at different β . Accordingly, such a complicated calibration is very difficult to accomplish when multiple anisotropic distributions simultaneously exist in practical applications. Fortunately, the “FINite slice Analysis” (FinA) method has been developed by Suits’ group recently,³⁴ in which the effective slice width can be determined. As a result, the corrections for the influence of finite slicing on velocity distributions extracted from a partially sliced image can be quantitatively performed.

IV. CONCLUSIONS

Generally, the 3D velocity distribution is easily derived from the common time-sliced velocity map images, with a high energy resolution. In comparison with the 2D VMI, the inverse Abel or Hankel transformations are no longer required for the time-sliced

images, thus eliminating the centerline noise in the reconstructed distributions. However, due to the weak extraction electric field, the common 3D VMI optics cannot provide a sufficient time resolution for distinguishing the adjacent m/z peaks in the TOF mass spectra. Thus, it is still a challenge to achieve a high time resolution and a high energy resolution in one VMI apparatus without the need to break the vacuum and reconnect the resistors.

In this work, we have proposed a convenient switch design for a high time resolution and a high energy resolution in a common 3D ion velocity imaging. By simply connecting two additional resistors (R_2' and R_8'), we have greatly increased the ratio of the electric field strengths of the extraction and acceleration stages, and the free drift region has significantly been extended without any change in the ion optics geometry. As an optimized result, the 2D VMI effect has been achieved with the higher time resolution, while maintaining the high energy resolution. As shown by the almost identical image patterns recorded with the 2D and 3D VMI modes and the generally consistent KERD curves, the feasibility of the designed 2D/3D switch is validated. Moreover, corrections on the measurement of branching ratios are discussed as well by comparing the 2D VMI and time-sliced images. Overall, the current ion optics design will be very useful in some special photodissociation or dissociative photoionization studies, in which the fragment ions with adjacent m/z are produced even with a certain kinetic energy distribution.

ACKNOWLEDGMENTS

This work was financially supported by the National Key Research and Development Program of China (Grant No. 2022YFF0707202) and the National Natural Science Foundation of China (Grant Nos. 22027801 and 22073088). T. Yu and X. Zhou are also grateful for the support of the Fundamental Research Funds for the Central Universities (Grant No. JZ2023HGQA0121).

AUTHOR DECLARATIONS

Conflict of Interest

The authors have no conflicts to disclose.

Author Contributions

Tongpo Yu: Conceptualization (equal); Data curation (equal); Formal analysis (lead); Investigation (equal); Methodology (equal); Writing – original draft (equal). **Xinlang Yang:** Data curation (equal); Investigation (equal). **Zhi Gao:** Formal analysis (equal). **Baokun Shan:** Data curation (equal); Investigation (equal). **Lei Xu:** Data curation (equal); Formal analysis (equal). **Xiaoguo Zhou:** Investigation (equal); Project administration (equal); Supervision (equal); Writing – review & editing (equal). **Shilin Liu:** Funding acquisition (equal); Project administration (equal); Supervision (equal).

DATA AVAILABILITY

All relevant data are within the paper.

REFERENCES

- 1 D. W. Chandler and P. L. Houston, “Two-dimensional imaging of state-selected photodissociation products detected by multiphoton ionization,” *J. Chem. Phys.* **87**, 1445 (1987).
- 2 A. T. J. B. Eppink and D. H. Parker, “Velocity map imaging of ions and electrons using electrostatic lenses: Application in photoelectron and photofragment ion imaging of molecular oxygen,” *Rev. Sci. Instrum.* **68**, 3477 (1997).
- 3 A. J. R. Heck and D. W. Chandler, “Imaging techniques for the study of chemical reaction dynamics,” *Annu. Rev. Phys. Chem.* **46**, 335 (1995).
- 4 P. L. Houston, “Snapshots of chemistry: Product imaging of molecular reactions,” *Acc. Chem. Res.* **28**, 453 (1995).
- 5 A. G. Suits and R. E. Continetti, *Imaging in Chemical Dynamics* (American Chemical Society, Washington, DC, 2001).
- 6 B. J. Whitaker, *Imaging in Molecular Dynamics: Technology and Applications* (Cambridge University Press, Cambridge, 2003).
- 7 V. Dribinski, A. Ossadtchi, V. A. Mandelshtam, and H. Reisler, “Reconstruction of Abel-transformable images: The Gaussian basis-set expansion Abel transform method,” *Rev. Sci. Instrum.* **73**, 2634 (2002).
- 8 C. R. Gebhardt, T. P. Rakitzis, P. C. Samartzis, V. Ladopoulos, and T. N. Kitsopoulos, “Slice imaging: A new approach to ion imaging and velocity mapping,” *Rev. Sci. Instrum.* **72**, 3848 (2001).
- 9 D. Townsend, M. P. Minitti, and A. G. Suits, “Direct current slice imaging,” *Rev. Sci. Instrum.* **74**, 2530 (2003).
- 10 K. T. Lorenz, D. W. Chandler, J. W. Barr, W. Chen, G. L. Barnes, and J. I. Cline, “Direct measurement of the preferred sense of NO rotation after collision with argon,” *Science* **293**, 2063 (2001).
- 11 T. Kinugawa and T. Arikawa, “Three-dimensional velocity analysis combining ion imaging with Doppler spectroscopy: Application to photodissociation of HBr at 243 nm,” *J. Chem. Phys.* **96**, 4801 (1992).
- 12 J. J. Lin, J. Zhou, W. Shiu, and K. Liu, “Application of time-sliced ion velocity imaging to crossed molecular beam experiments,” *Rev. Sci. Instrum.* **74**, 2495 (2003).
- 13 J. H. Jungmann, A. Gijssbertsen, J. Visser, J. Visschers, R. M. A. Heeren, and M. J. J. Vrakking, “A new imaging method for understanding chemical dynamics: Efficient slice imaging using an in-vacuum pixel detector,” *Rev. Sci. Instrum.* **81**, 103112 (2010).
- 14 A. T. Clark, J. P. Crooks, I. Sedgwick, R. Turchetta, J. W. L. Lee, J. J. John, E. S. Wilman, L. Hill, E. Halford, C. S. Slater, B. Winter, W. H. Yuen, S. H. Gardiner, M. L. Lipciuc, M. Brouard, A. Nomerotski, and C. Vallance, “Multimass velocity-map imaging with the pixel imaging mass spectrometry (PIImMS) sensor: An ultra-fast event-triggered camera for particle imaging,” *J. Phys. Chem. A* **116**, 10897–10903 (2012).
- 15 M. Fisher-Levine, R. Boll, F. Ziaee, C. Bomme, B. Erk, D. Rompotis, T. Marchenko, A. Nomerotski, and D. Rolles, “Time-resolved ion imaging at free-electron lasers using TimepixCam,” *J. Synchrotron Radiat.* **25**, 336–345 (2018).
- 16 Y. Zhang, C.-H. Yang, S.-M. Wu, A. van Roij, W. J. van der Zande, D. H. Parker, and X. Yang, “A large aperture magnification lens for velocity map imaging,” *Rev. Sci. Instrum.* **82**, 013301 (2011).
- 17 D. A. Horke, G. M. Roberts, J. Lecointre, and J. R. R. Verlet, “Velocity-map imaging at low extraction fields,” *Rev. Sci. Instrum.* **83**, 063101 (2012).
- 18 B. Y. Chang, R. C. Hoetzlein, J. A. Mueller, J. D. Geiser, and P. L. Houston, “Improved two-dimensional product imaging: The real-time ion-counting method,” *Rev. Sci. Instrum.* **69**, 1665 (1998).
- 19 G. A. Garcia, L. Nahon, and I. Powis, “Two-dimensional charged particle image inversion using a polar basis function expansion,” *Rev. Sci. Instrum.* **75**, 4989 (2004).
- 20 W. Li, S. D. Chambreaux, S. A. Lahankar, and A. G. Suits, “Megapixel ion imaging with standard video,” *Rev. Sci. Instrum.* **76**, 063106 (2005).
- 21 M. N. R. Ashfold, N. H. Nahler, A. J. Orr-Ewing, O. P. J. Vieuxmaire, R. L. Toomes, T. N. Kitsopoulos, I. A. Garcia, D. A. Chestakov, S. M. Wu, and D. H. Parker, “Imaging the dynamics of gas phase reactions,” *Phys. Chem. Chem. Phys.* **8**, 26 (2006).
- 22 A. I. Chichinin, K. H. Gericke, S. Kauczok, and C. Maul, *Int. Rev. Phys. Chem.* **28**, 607 (2009).

- ²³S. J. Greaves, R. A. Rose, and A. J. Orr-Ewing, "Velocity map imaging of the dynamics of bimolecular chemical reactions," *Phys. Chem. Chem. Phys.* **12**, 9129 (2010).
- ²⁴Z. Luan, Y. Fu, Y. Tan, Y. Wang, B. Shan, J. Li, X. Zhou, W. Chen, L. Liu, B. Fu, D. H. Zhang, X. Yang, and X. Wang, "Observation of competitive nonadiabatic photodissociation dynamics of H_2S^+ cations," *J. Phys. Chem. Lett.* **13**, 8157 (2022).
- ²⁵G. Wu, W. Zhang, H. Pan, Q. Shuai, B. Jiang, D. Dai, and X. Yang, "A new crossed molecular beam apparatus using time-sliced ion velocity imaging technique," *Rev. Sci. Instrum.* **79**, 094104 (2008).
- ²⁶X. Tang, X. Zhou, M. Niu, S. Liu, J. Sun, X. Shan, F. Liu, and L. Sheng, "A threshold photoelectron-photoion coincidence spectrometer with double velocity imaging using synchrotron radiation," *Rev. Sci. Instrum.* **80**, 113101 (2009).
- ²⁷D. H. Parker and A. T. J. B. Eppink, "Photoelectron and photofragment velocity map imaging of state-selected molecular oxygen dissociation/ionization dynamics," *J. Chem. Phys.* **107**, 2357 (1997).
- ²⁸W. Qi, P. Jiang, D. Lin, X. Chi, M. Cheng, Y. Du, and Q. Zhu, "A mini-photofragment translational spectrometer with ion velocity map imaging using low voltage acceleration," *Rev. Sci. Instrum.* **89**, 013101 (2018).
- ²⁹X. Wu, Z. Gao, T. Yu, G. Zhou, and S. Liu, " $\text{S}(^3\text{P})$ fragmentation channel of carbonyl sulfide at 230 nm," *Acta Phys. Chim. Sin.* **33**, 2004 (2017).
- ³⁰A. Sugita, M. Mashino, M. Kawasaki, Y. Matsumi, R. Bersohn, G. Trott-Kriegeskorte, and K. H. Gericke, "Effect of molecular bending on the photodissociation of OCS," *J. Chem. Phys.* **112**, 7095 (2000).
- ³¹H. Katayanagi and T. Suzuki, "Non-adiabatic bending dissociation of OCS: The effect of bending excitation on the transition probability," *Chem. Phys. Lett.* **360**, 104 (2002).
- ³²M. L. Lipciuc and M. H. Janssen, "Slice imaging of the quantum state-to-state cross section for photodissociation of state-selected rovibrational bending states of $\text{OCS}(\nu_2 = 0, 1, 2|JIM) + h\nu \rightarrow \text{CO}(J) + \text{S}(^1\text{D}_2)$," *J. Chem. Phys.* **126**, 194318 (2007).
- ³³D. Townsend, S. A. Lahanker, S. K. Lee, S. D. Chambreau, A. G. Suits, X. Zhang, J. Rheinecker, L. B. Harding, and J. M. Bowman, "The roaming atom: Straying from the reaction path in formaldehyde decomposition," *Science* **306**, 5669 (2004).
- ³⁴J. O. F. Thompson, C. Amarasinghe, C. D. Foley, and A. G. Suits, "Finite slice analysis (FINA)—A general reconstruction method for velocity mapped and time-sliced ion imaging," *J. Chem. Phys.* **147**, 013913 (2017).